Friction and wear of AISI 304 by the SiC ball and its monitoring via Barkhausen noise emission

M. Neslušan [a,*], J. Bronček [a], P. Minárik [b,c], J. Čapek [d], M. Vicen [a], M. Drbúl [a]

[a] *University of Žilina, Faculty of Mechanical Engineering, Univerzitná 1, 010 26, Žilina, Slovakia*
[b] *Charles University, Faculty of Mathematics and Physics, Ke Karlovu 5, 121 16 Praha 2, Czech Republic*
[c] *University of Žilina, Research Centre, Univerzitná 8215/1, 010 26, Žilina, Slovakia*
[d] *Czech Technical University in Prague, Faculty of Nuclear Sciences and Physical Engineering, Trojanova 13, 120 00 Praha, Czech Republic*

A B S T R A C T

This study deals with the friction and wear of AISI 304 austenitic steel by the SiC ball. The surface state in the affected region was investigated as a function of the time duration of the friction process due to a single ceramic spherical SiC ball tip in a reversible linear motion under a load of 10 N (ball-on-flat test method). Only minor alterations in the loaded region could be found in the initial phase of friction, which was followed by an abrupt increase in the size of the wear track produced. Wear tracks were investigated in terms of their size, residual stress state, phase composition, delamination, and chemistry. Due to the phase transformation from austenite to martensite, the magnetic Barkhausen noise technique was also employed, and its sensitivity to alterations arising during friction and wear was investigated. It was found that magnetic Barkhausen noise was sensitive to the volume fraction of strain-induced martensite. Moreover, pronounced surface oxidation could be detected in the region of surface delamination, in contrast to the initial phase of friction.

1. Introduction

Austenitic steels are frequently employed in a variety of applications with high requirements for a combination of factors, such as corrosion resistance, toughness, fatigue, and/or resistance against chemical attacks [1,2]. The high plasticity of these steels is linked to the fcc (face-centred cubic) lattice and the corresponding multiple slip system of dislocation motion [3]. The microstructure of steels with respect to their phase is strongly affected by the alloying elements, as summarised in the Schaeffler-Delong diagram. Hence, the presence of an austenite phase is mainly due to the predominance of austenite stabilisers, such as Ni, C, N, Mn, Cu, and Co, over ferrite stabilisers, such as Cr, Si, and Mo [1]. However, austenite should still be considered a metastable phase since a strain-induced martensite transformation can be detected during the component manufacturing process or under load in real industrial applications [4–7]. Furthermore, a loss of corrosion resistance can be found at elevated temperatures in some applications [1,2].

Austenite is a paramagnetic phase, in contrast to strain-induced martensite, which is strongly ferromagnetic. The lattice transformation from fcc to bcc (body-centred cubic) in austenitic steels drastically changes their magnetic properties. For this reason, magnetic

techniques such as magnetic Barkhausen noise (MBN) have the potential to be employed to monitor this transition [4,8,9]. The formation of a magnetic domain substructure and the corresponding domain walls (DWs) results in the emission of electromagnetic pulses produced by the DWs under an altered magnetic field [10–12]. The clustered, irreversible motion of the DWs and the corresponding pulses can be detected at the free surface as MBN. The main advantage of the MBN technique in terms of monitoring the strain-induced martensite transformation in austenitic steels is associated with the lack of MBN in paramagnetic austenite. Hence, the MBN emissions can be directly linked with strain-induced martensite (its fraction, preferential orientation, etc.) [4,8,9]. It should be noted that an MBN sensing probe produces its own MBN signal, which can be easily detected and subtracted [13].

The friction process and the corresponding wear can be investigated under laboratory conditions using professional or self-made devices in different modes. Using a small single tip of spherical shape to perform linear, backward reversible motion (the ball-on-flat test method) can significantly alter the surface state in the wear track. A small load (commonly only 10 N) is concentrated in a narrow region, producing high local stresses of hundreds of MPa or GPa [14]. The compounding effects of elevated temperature should also be considered since the

energy consumed at the interface between the tip and surface is converted into heat [14]. For these reasons, it is reasonable to expect instability in austenite, as well as alterations in the corrosion resistance of austenitic steels under friction and developed wear, as proved in earlier studies [15–19] that have investigated the influence of load, temperature, sliding velocity, time duration, etc. Related information can also be collected from studies focused on retained austenite embedded in the ferrite and/or martensite [20,21]. The phase transformation of austenite - martensite, which also involves a magnetic transformation from a paramagnetic - ferromagnetic body, suggests that a suitable magnetic technique could be employed to investigate this topic. The primary motivation and novelty of our study lie in the employment of MBN emission as a prospective and beneficial technique for the fast and reliable detection of alterations in the region of the wear track produced by the friction process for components made of austenitic steel.

2. Experimental method

Experiments were carried out on AISI 304 austenitic steel delivered in the form of a sheet (3 mm thick). The nominal chemical composition of this steel is shown in Table 1. Its mechanical and other properties were as follows: yield strength 190 MPa, ultimate strength 600 MPa, elongation at break 45%, thermal conductivity 16.2 $Wm^{-1}K^{-1}$. The sheet surface was smoothed by cold rolling, which introduced about 10% of strain-induced martensite in the near-surface layer, with a thickness of about 10 μm. In addition, the effect of cold rolling on the bulk microstructure was twofold. Firstly, approximately 2% of the strain-induced martensite was found randomly distributed across the sheet thickness. Secondly, the bulk stress in austenite along the cold rolling direction was measured to be -115 ± 16 MPa and the crystallite size was estimated to be 50.5 ± 0.5 nm. These measurements were performed by X-ray diffraction (XRD) on the electrochemically etched surfaces in the preliminary phase of the investigations.

Samples of length 70 mm and width 20 mm were cut from the sheet, and the surface layer containing strain-induced martensite originating from cold rolling was removed by electrochemical etching. The samples were masked with plastic tape, and an area of width of about 10 mm and length of about 60 mm was left free, which was subjected to electrolytic etching in 20% H_2SO_4 solution for 10 min (etching voltage 6 V and current 4.5 A, etching off a layer with thickness about 50 μm). The friction test was carried out in the etched region only to avoid a mixture of strain-induced martensite originating from cold rolling, friction and developed wear (see Fig. 1).

The friction tests were conducted under atmospheric conditions without the presence of a lubricant. The air humidity was not measured. The dry friction coefficient was determined using a self-made linear tribometer (see Fig. 2) by the ball-on-flat test method (where the friction force F_S was measured using the strain gauge technique). During these tests, the SiC ball (diameter 3.16 mm) was loaded with a normal force $F_N = 10$ N, with a sliding speed of 0.017 ms^{-1} (reversible linear motion). The experimental data obtained from the linear tribometer were processed using the NI DIADEM program. The test was varied as a function of time, and the linear motion was stopped after the predefined periods shown in Table 2. For each time period, three repetitive measurements were carried out, and a new SiC ball was employed for each repetitive test. Due to the significantly higher hardness of the SiC balls compared with the AISI 304, the influence of ball wear was neglected (the surface of the ball was also screened).

MBN is sensitive to both the stress state (the realignment of DWs with

respect to stress [22,23]) and the microstructure since DWs are pinned by lattice imperfections such as dislocations, precipitates, non-ferromagnetic phases, etc. [24–26]. It is also sensitive to the surface heights of irregularities and the corresponding propagation of electromagnetic pulses toward the sensing coil [27]. For these reasons, the residual stresses in the martensite and austenite phases were determined through the use of XRD, and the relative strengthening of the wear track was analysed based on microhardness measurements. This technique also provides specific information about the microstructure expressed in terms of phase fractions and their microstress/microstrain. Shape factors and surface topography were investigated using SEM (scanning electron microscopy, which also provides information on chemical composition as well as) using an Alicona 5.

The surface roughness parameters Ra and Rz, measured across and along the wear track, were calculated from the measured wear track profiles according to ISO 4288:1998. Therefore, the cut-off wavelengths of 0.25 mm ($Rz < 0.5$ μm) and 0.8 mm ($Rz > 0.5$ μm) were used for the Rz calculation. Measurements of the wear track widths were carried out using Zeiss AxioCam MRc5 and Olympus SZx16 light microscopes with Quick Photo Industrial 3.0 software. Each wear track width was obtained by averaging five measurements.

The microstructure and chemical composition profiles of the samples were investigated by SEM ZEISS Auriga Compact equipped with an EDAX energy-dispersive X-ray spectroscope. The investigation of the cross-section of the wear track was performed on samples, which were embedded in the epoxy resin, mechanically polished and electrochemically etched (Struers Lectropol, Struers A3 solution). Note that two types of the signal were detected: the secondary electrons (SE, sensitive to topography) and the backscattered electrons (BSE, sensitive to composition and matrix orientation).

A finite element model was used to simulate the distribution of temperature at the sample – SiC ball interface. For the simulation, the same experimental conditions as for the wear test were used. The thermo-mechanical model was solved with Abaqus/Explicit software. The materials' parameters shown in Table 3 were used for the numerical model and the sliding velocity was selected to be 0.02 m s^{-1}. The net of elements of size 10 μm was employed in the contact of the bodies and the size of elements was minimized with respect of singularities in the model.

An X'Pert PRO MPD diffractometer was used for the XRD measurements. The lattice deformations in the austenite and ferrite phases were investigated using manganese (for the austenite phase) and chromium radiation (for the ferrite phase), with average effective penetration depths of approximately 5.5 (for the austenite phase) and 4 μm (for the austenite phase), respectively. The diffraction angles were determined from the peaks in the diffraction lines $K\alpha_1$ for the {311} and {211} planes of the austenite and ferrite phases, and were fitted with the Pearson VII function and Rachinger's method for the separation of the diffraction lines $K\alpha_1$ and $K\alpha_2$. To determine the residual stresses, the Winholtz and Cohen method and X-ray elastic constants $\frac{1}{2}s_2 = 7.18$ TPa^{-1}, $s_1 = -1.2$ TPa^{-1} and $\frac{1}{2}s_2 = 5.75$ TPa^{-1}, $s_1 = -1.25$ TPa^{-1} were used for the austenite and ferrite phases, respectively. In addition, the measured XRD patterns were used for quantification of dislocation density in austenite and martensite phases employing the Williamson-Hall analysis [28]. Table 4 shows the constants used for the Williamson-Hall analysis.

The crystallite size (i.e., the size of coherently diffracted domains) was determined from the XRD patterns obtained using cobalt radiation, and the subsequent Rietveld refinement was performed with MStruct software. The average effective penetration depth of the XRD measurements was approximately 6.2 μm. Using the XRD data, the crystallite size t was calculated based on the Scherrer formula (Equation (1)):

$$t = K.\lambda/(B.\cos\theta), \tag{1}$$

where K, λ, B, and θ are the shape factor, X-ray wavelength, diffraction

Table 1
Nominal chemical composition of AISI 304 (wt. %).

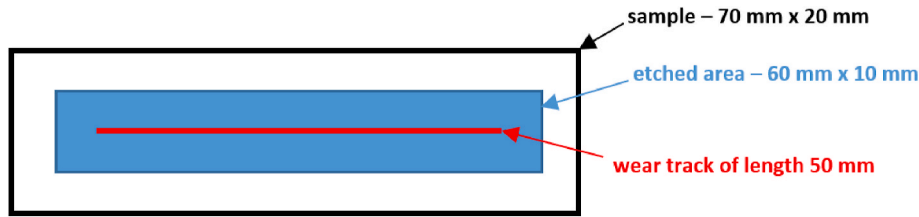| Fe	C	Mn	Si	Cr	S	P	N	Ni
balance	0.07	2.00	1.00	18.50	0.03	0.05	0.11	9.25

Fig. 1. Brief illustration of sample used for friction test.
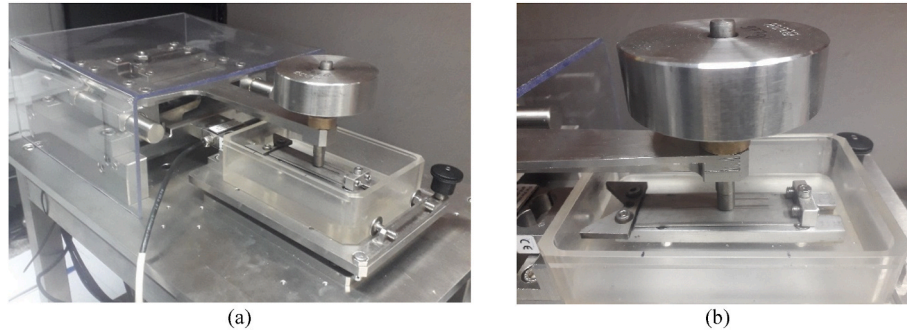

(a) (b)

Fig. 2. (a) Self-made device and (b) detail of the sample with the load.

Table 2
Predefined times (in minutes) and the corresponding sliding distance used for the friction process.

time, min	1	5	7.5	15	20	25	30	40	50	60
sliding distance, m	1.02	5.10	7.65	15.30	20.40	25.50	30.60	40.80	51.00	61.20

Table 3
The parameters used in the finite element model simulation.

	Austenite steel	SiC ball
Thermal conductivity, $W.m^{-1}.K^{-1}$	16.2	90.0
Density, $kg.m^{-3}$	7850	3210
Young's modulus, MPa	190 000	400 000
Poisson's ratio, -	0.3	0.16
Specific heat, $J.kg^{-1}.K^{-1}$	466	660

Table 4
The constants used for the Williamson-Hall analysis.

	martensite	austenite
Constant K,-	14.4	16.1
Lattice parameter a, nm	0.288081	0.3591
Burgers vector b, nm	0.249485	0.253922

peak broadening and diffraction angle, and the Bragg angle, respectively ($K = 1$ and $\lambda = 0.1790307$ nm). The irradiated volume was defined based on experimental geometry, the effective penetration depth, and the pinhole size (0.25 × 1 mm).

Optical observations of the topography of the wear track and their corresponding profiles were carried out using an Alicona InfiniteFocus G5 (focus-variation technology, TU Plan ELWD lens, magnification 50×, white polarised light). The obtained data were post-processed using external Surfcom Map Standard software. The microhardness (*HV0.2*) was measured at the centre of the wear track (Innova Test 400TM, 200 g for 10 s, five measurements for each notch).

The MBN electromagnetic pulses were initiated under an alternating magnetic field (± 9.87 kA m^{-1}) with a sine profile and frequency 125 Hz, using a RollScan 350 (serial sensor S1-18-12-01, Stresstech Oy manufacturer). The alternating magnetic field was distributed along the

length of the wear track. The signals were recorded, filtered in order to suppress the low-frequency components (only MBN pulses in the frequency range 20–1000 kHz were allowed), and visualised using MicroScan 600 software. Due to the low amplitude of the electromagnetic pulses originating from the surface (which was comparable with the emission of MBN originating from the background noise produced by the sensor [13]), all the filtered signals were exported and analysed using self-made software specially developed for this purpose. Only pulses outside the background noise of 70 mV were employed for further calculations of the effective value of the signals referred to as MBN (in mV), and in the reconstruction of the MBN envelopes. *PP* (peak position) and *FWHM* (Full Width at Half Maximum) were proposed as suitable parameters extracted from MBN envelopes. *PP* refers to the position of the maximum of the MBN envelope in a magnetic field, whereas *FWHM* is the full width at half maximum of the MBN envelope. The MBN parameters were obtained by averaging 10 consecutive MBN bursts.

3. Experimental results and discussion

3.1. SEM observations, chemical analyses and temperature simulation

The Hertz model for the contact between solid elastic bodies can be employed to analyse the processes occurring during the ball-on-flat test method [14,29]. For a ball of radius r (1.58 mm) on a flat surface, the maximum contact pressure p_{max} under a normal load F_N (10 N) can be calculated as follows:

$$p_{max} = \frac{3F_N}{2\pi r^2} \tag{2}$$

However, the mean pressure p_m is lower:

$$p_m = \frac{2}{3} p_{max} \tag{3}$$

Mohr specified the criteria for which elastic deformation is replaced by plastic behaviour based on a threshold surface critical shear stress τ_{cr}

$$\tau_{max} \geqq \tau_{cr} = \frac{R_e}{2} \tag{4}$$

where R_e represents the yield stress of the material.

Plastic deformation is initiated as soon as p_{max} attains a value of $3.1\tau_{cr}$, or when p_m reaches the yield strength. Macroscopic plastic deformations appear on the surface when $p_m \geq 3R_e$.

For our values of $R_e = 190$ MPa, initial $p_{max} = 2.12$ GPa, and $p_m = 1.41$ GPa, it can easily be seen that the conditions for considerable plastic deformation are met. Consequently, the plastic deformation of the surface occurs in the initial phase of the test, as shown in Fig. 3. The figure also illustrates the remarkable difference in the appearance of the wear track as a function of the duration of the friction process. Fig. 3a (see also Fig. 4a) shows that the surface of the wear track is smooth, with protrusions at its edges. These pile-ups are due to the extrusion of friction pairs, as observed previously in Ref. [21]. A ploughing mechanism of friction predominates, and the wear volume is very limited. It is reasonable to assume that the plastic deformation in this phase accumulates in the wear track via the initiation of dislocation slips (possibly via a twinning mechanism) and the corresponding strain hardening. As soon as the accumulated energy in the surface and subsurface region attains the critical threshold (i.e., the multiple slip system is fully consumed), surface delamination is seen and significant alterations with respect to the size and appearance of the produced wear tracks can be detected, as shown in Fig. 3b and c and Fig. 4a–f. These figures also show friction debris, grooves, and surface cracking.

In the Hertz theory of stress distribution with respect to the surface depth, it is assumed that microcracks are initiated in the subsurface region and propagate towards the free surface. A superimposed contribution from friction heating will also be encountered due to repetitive surface heating followed by rapid self-cooling. The significant contribution of thermal cycling to surface degradation is driven by the low thermal conductivity of austenite. The weak heat transfer from the heated surface towards the deeper, colder subsurface means that the temperatures in the thin local zones of the friction contact are high. The presence of spherical debris on the surface (see Fig. 4e and f) indicates that the melting temperature was locally reached.

Fig. 5 demonstrates the simulated distribution of temperature in the contact region of the sample – SiC ball during the wear test. As shown, the temperature field is heterogeneous – attaining the maxima in the wear track centre and steeply decreasing perpendicularly to the sliding direction. For this reason, the influence of the heat generated during the wear test would remarkably vary across the wear track width. The thermal softening effect is expected to be less pronounced near the wear track boundary than at the wear track centre. In addition, the simulation showed that the temperature at the wear track centre could exceed the melting point of the studied material. It is also expected that the phase transformation just underneath the wear track can be affected by a combination of high strain and short-term high temperature. Consequently, the martensite, which forms underneath the wear track, may be strain-induced (resulting from high local strains) as well as temperature induced (resulting from short exposure to high temperature followed by fast self-cooling).

High temperatures also promote surface oxidation (corrosion). Fe oxides usually appear in SEM secondary electron (SE) images as bright spots against a much darker non-corroded matrix. Fig. 3 clearly shows that corrosion damage increases with the accumulation of friction damage. Only a few areas can be found in the extruded pile-ups in the ploughing phase (see Fig. 3a); however, as soon as delamination takes place, oxidation is enormously accelerated and occurs not only in the extruded pile-ups but also in the wear track. Fig. 3 shows that the degree of surface oxidation increases throughout the friction process.

Fig. 6 illustrates a cross-section of the wear track after 60 min at its centre. In Fig. 6a, cracked surface oxides appear dark grey (EDS analysis not shown here) and can be easily distinguished from the much brighter underlying layer, unaffected by the oxidation. Note that the contrast of oxides in BSE (Fig. 6) is the opposite of in SE (Fig. 4). Clearly, the thickness of the oxide layer varies and does not cover the whole wear track. Fig. 6b shows the detail of the sub-surface layer. It is obvious that a high plastic deformation was introduced to the sample during the wear test and the uppermost layer was heavily deformed. The extent of the deformation abruptly decreases with an increasing distance from the surface. The typical shear bands corresponding to the strain-induced martensite are visible in the less deformed zone. The thickness of the heavily deformed layer containing a high volume fraction of martensite varies from 5 up to 30 μm.

Surface oxidation can also be proved by chemical analysis, as shown in Fig. 7. The relative intensities of O, Fe, and Cr were shown to be nearly unchanged through a comparison of the intensities outside and inside of the wear track before delamination (although a slight increase in O can be found at the edge of the wear track, as mentioned above). On the other hand, a remarkable enrichment in O at the expense of Fe was found in the final phases of the friction process. Similar behaviour was reported by Hua [19]. Fig. 3c illustrates the asymmetric distribution of the bright-dark contrast within the wear track width. However, in Fig. 7b, a less pronounced asymmetry can be seen; this mimics the expected distribution of local stress, where the maximum relative intensity of O can be found near the centre of the wear track, and there is a progressive decrease toward the edges of the wear track.

3.2. Profile measurements and friction coefficient

Visual observations of the wear track surface and the corresponding wear track profile, as illustrated in Figs. 8 and 9, clearly depict a smooth surface with much lower depths and heights of irregularities in the wear track after the ploughing phase. As soon as the ploughing - delamination transition takes place, the surface becomes very rough due to the delamination of the wear track. The heights of the irregularities in the wear track after this transition are driven by the heterogeneity of delamination across both the width and length of the wear track, where the heavily delaminated regions adjoin less affected areas containing furrows and microcracks (see especially Fig. 4d,f). Peeled lamellas also
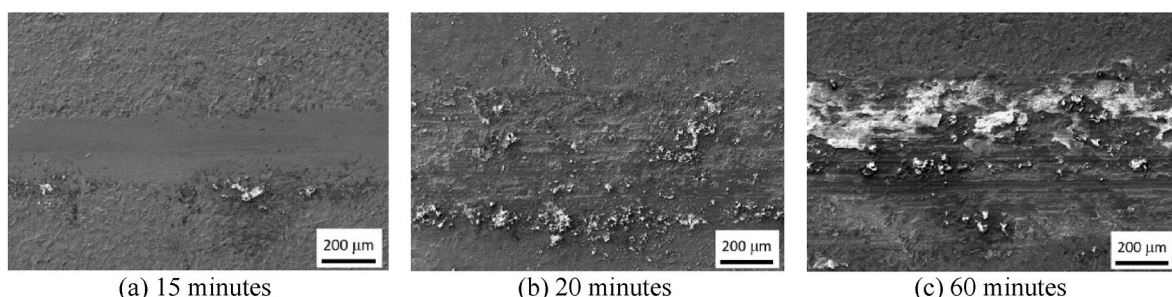

(a) 15 minutes   (b) 20 minutes   (c) 60 minutes

Fig. 3. SEM images of the surface after testing.

(a) 15 minutes   (b) 20 minutes

(c) 20 minutes - detail   (d) 40 minutes

(e) 60 minutes   (f) 60 minutes - detail
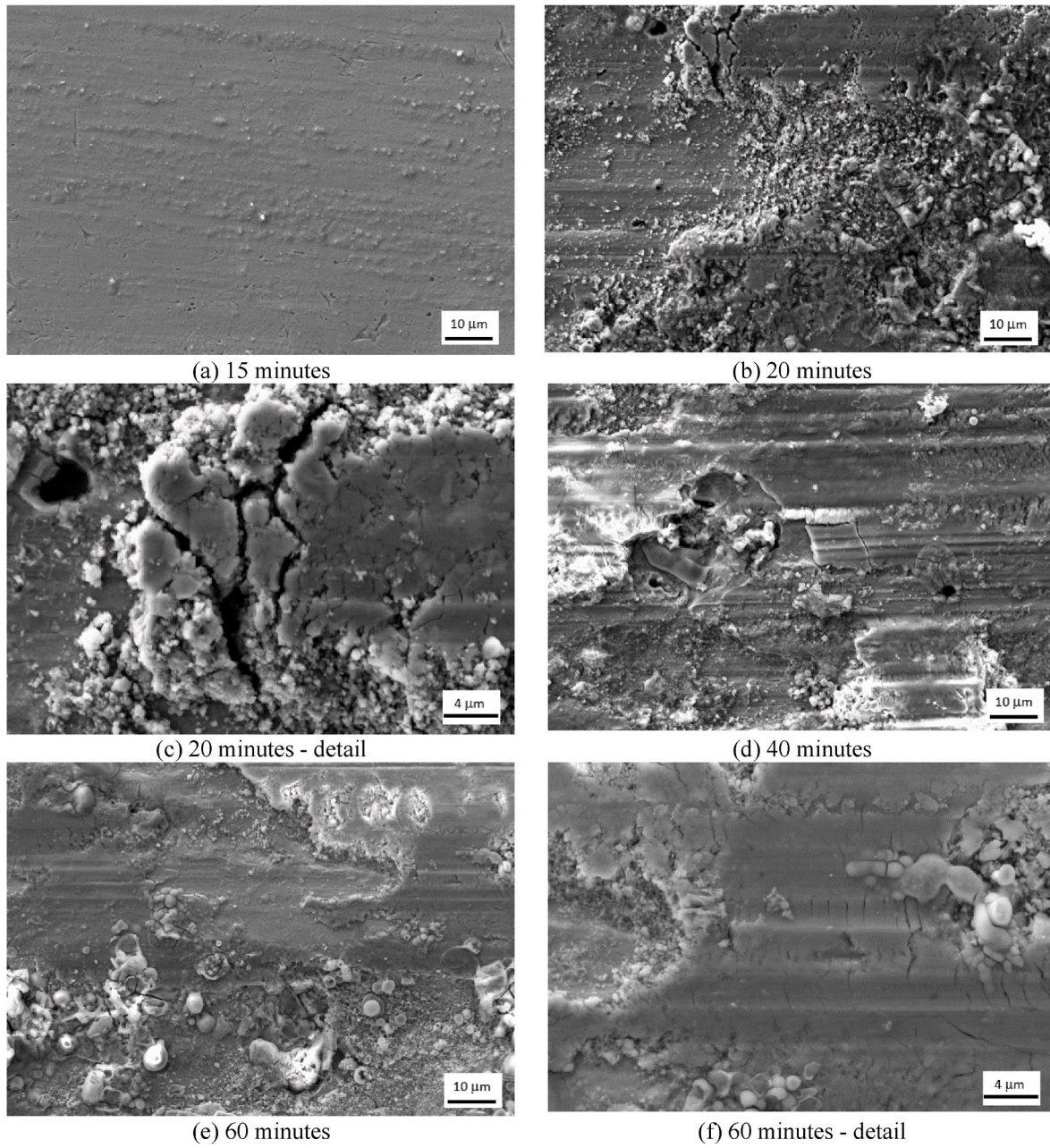
Fig. 4. SEM details of the surface after testing (SEM, SE).

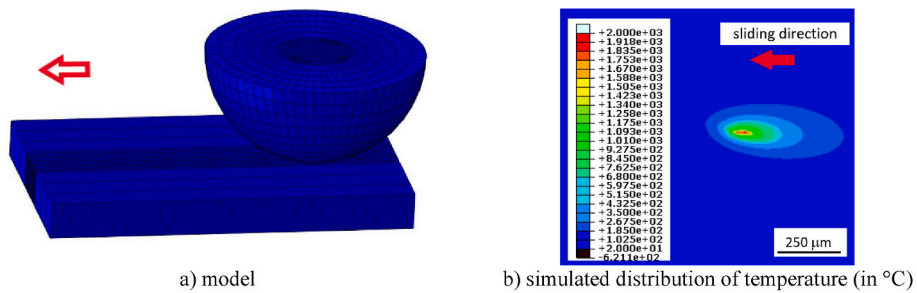a) model   b) simulated distribution of temperature (in °C)

Fig. 5. Distribution of temperature obtained from the software Abaqus explicit after 1 min of friction.

adhere to the worn surface and contribute to surface roughening [19, 21]. Delamination and adhesion make visual observation a relatively difficult and complex task since this effect makes the contrast between the wear track and the unaffected surfaces less apparent (see also Figs. 8b and 9b).

Fig. 10 shows that the surface of the wear track is being smoothed

a) SEM image of the surface

b) detail
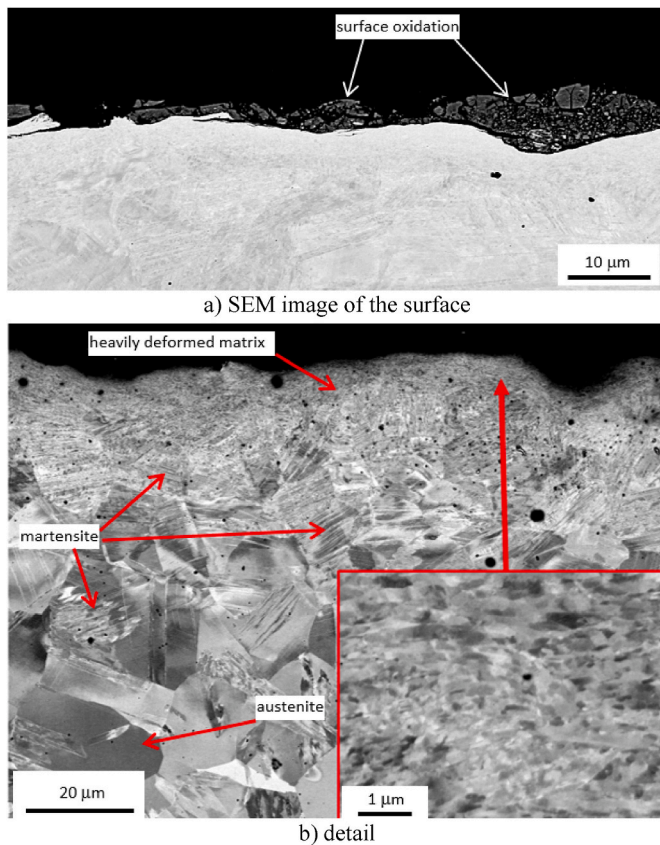
Fig. 6. Cross-sectional SEM views at the centre of the wear track after 60 min (SEM, BSE).

during the ploughing period, followed by an abrupt increase in topography once the delamination is initiated. There is a significant increase in both *Ra* and *Rz* parameters during the delamination period since the surface is composed of microcracks and peeled/adhered lamellae. Moreover, the delamination is not uniform within the wear track and the delaminated regions are formed next to the less affected ones, see Fig. 4. The complex evolution of *Ra* and *Rz* parameters in the delamination period is caused by the aforementioned heterogeneity together with the avalanche-like character of the delamination process. The increasing topography expressed by *Ra* and *Rz* parameters (mainly due to adhesion of peeled lamellae) makes the contrast between the wear track (and its profile) and the unaffected region weaker, see also Figs. 8b and 9b.

Fig. 11 illustrates the close correlation between the phase of surface damage, the friction coefficient, and the width of the wear track. The lower friction coefficient in a wear track of low width is associated with ploughing wear, whereas the acceleration in the growth of the friction coefficient and the dramatic increase in the width of the wear track are linked with the transition from ploughing to the delimitation phase. The smooth surface of the wear track is replaced by a strongly abraded surface with significant heights of irregularities (see Figs. 3, 4, 8 and 9). Fig. 11 also shows that the steep changes arising from this transition are replaced by a saturation phase in which both the friction coefficient and the width of the wear track develop.

3.3. XRD and microhardness measurements

The near-surface agglomerates of martensite originating from cold rolling were etched off in the preliminary phase of the experiments, as described above. However, detailed screening of the bulk samples revealed a fraction of martensite of about 1.7%, randomly distributed across the widths of the samples. The significant martensite

transformation originating from the friction process could only be detected in the early phases of the ploughing phase (see Fig. 12), and arose as a result of the metastability of austenite, which is prone to a martensite transformation under mechanical load. The martensite fraction grew almost linearly during ploughing, followed by an abrupt increase in the ploughing - delamination transition. This transition also aligns with the significant growth in the friction coefficient as the smooth surface of the wear track becomes heavily abraded, containing debris, grooves, and pits (see Figs. 3 and 4).

We assume that the decreasing crystallite size of austenite (see Fig. 13b) was caused by the dislocation slip and the accumulation of dislocation tangles underneath the wear track surface. This effect was further strengthened during the ploughing phase. A combined contribution of strain hardening of austenite and an increasing fraction of martensite on the material's strength is expected soon after the ploughing - delamination transition (at 20 and 30 min). Finally, the predominant effect of martensite on the strengthening of the wear track surface is due to austenite dynamic recovery, which is expressed as large crystallite sizes as a result of austenite tempering.

The abrupt increase in the martensite fraction at the phase transition coincides with a large increase in the friction coefficient and growth in the wear track width. The increasing friction coefficient and the corresponding shear stress can be directly linked with the increasing intensity of severe plastic deformation, which plays the main role in the phase transformation. Although the layer containing martensite that develops in the ploughing phase is removed from the wear track, the measured XRD patterns and determined martensite fraction indicate that this effect is only minor. It may be that the delamination phase produces new martensite quite early and/or that the layer containing martensite originating from the ploughing phase is not fully removed across its full thickness.

The changes in the friction coefficient, the width of the wear track, and the martensite fraction indicate that conditions in the SiC ball – surface interface tend to stabilise over time. The surface strengthening due to the mechanism of austenite strain hardening in the ploughing phase is metastable, unlike the mechanism based on the high fraction of martensite. After wear track strengthening due to the high martensite fraction had taken place, no further dramatic alterations in the friction coefficient and/or wear track size were detected. In other words, the bearing capacity of the surface layer depends on the presence of martensite rather than on the accumulation of dislocations as a result of their motion in austenite, as reported in Refs. [20,21]. It is also worth mentioning that the increase in friction heating also plays a certain role, as described above. The temperature cycle tempers the martensite and austenite produced during the previous cycle, and these elevated temperatures make the austenite phase more stable (cf [15,21]). This effect contributes to the decrease in the martensite fraction over the long term. However, the main effect should be viewed as arising from the decreasing contact pressure associated with the increase in the wear track width and irradiated width, as discussed later.

Fig. 13a shows that both austenite and martensite contain residual compressive stresses. The influence of the duration of the friction process is nearly none and the magnitude of stress in both phases does not exhibit significant changes. However, the residual compressive stresses in martensite are much higher than in austenite. Based on this information, it can be concluded that the residual stress in austenite is almost unaffected by the friction process or that the affected layer is very thin with respect to the penetration depth of XRD.

The calculated dislocation density in martensite seems to be nearly unaffected within the XRD penetration depth (see Fig. 14), whereas the dislocation density in austenite is inversely proportional to the crystallite size (see also Fig. 13b). The dislocation density in austenite grows up to 30 min following the progressive descent afterwards. The dislocation density in this particular case can be linked with the hardness of a body. Fig. 15 and Fig. 13b illustrate that the evolution of *HV0.2* fits better with the dislocation density in austenite. On the other hand, the change in the

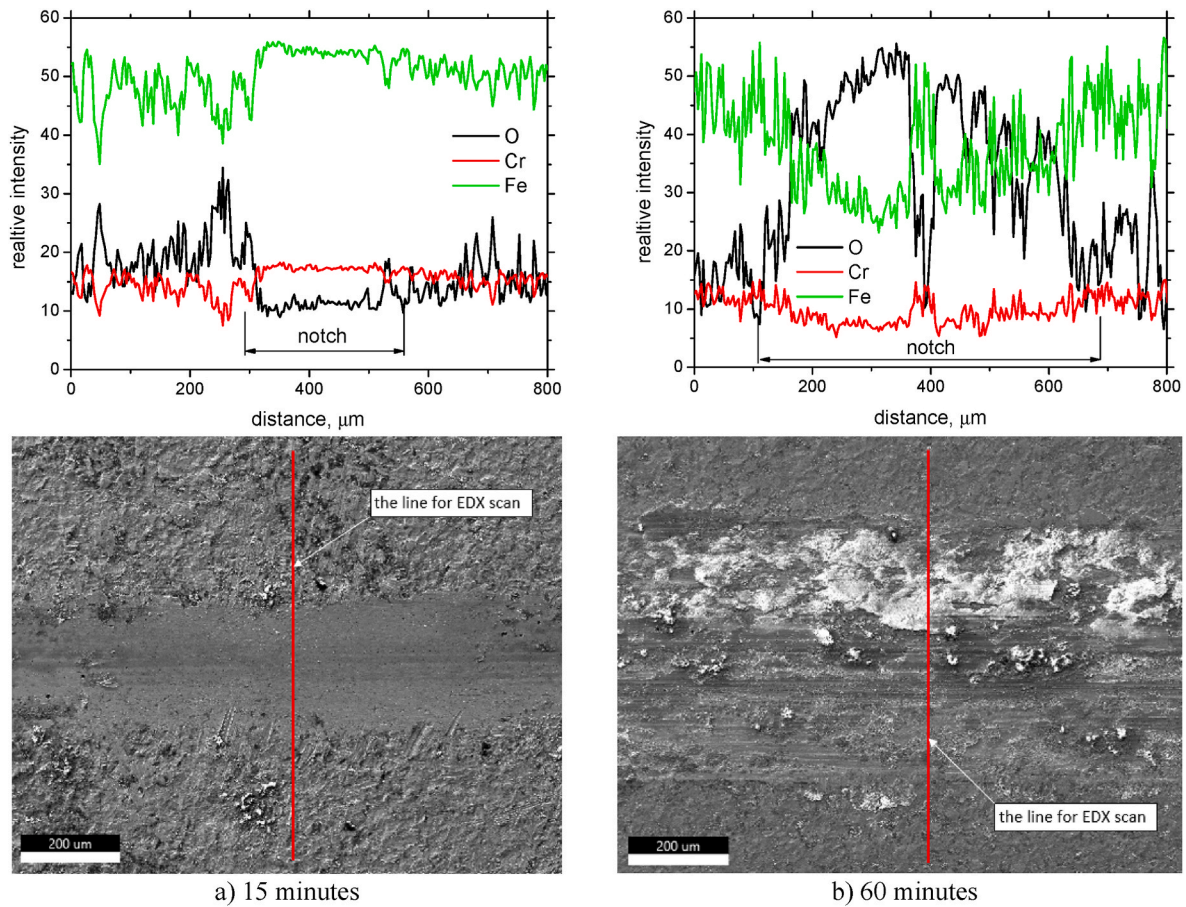a) 15 minutes

b) 60 minutes

Fig. 7. Results of chemical analyses: relative intensities of O, Fe and Cr across the wear track.
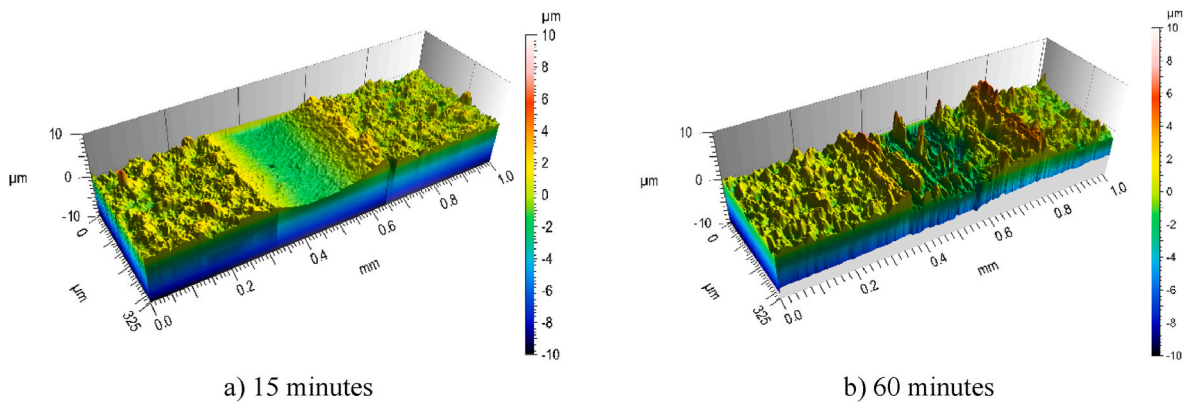

a) 15 minutes

b) 60 minutes

Fig. 8. Surface topography.

microhardness *HV0.2* (Fig. 15) is also quite similar to the change in the martensite fraction (for this reason, the limited XRD sensing depth takes a certain role), which also indicates that surface strengthening due to the austenite - martensite phase transformation is greater than for austenite strain hardening.

Note that the measured microhardness represents relative information about the wear track strengthening since during the 10 s application of the load, the tip penetrates through the thin near-surface layer in which both the phase fraction and their extent to the depth varies – valuable gradient expected (microhardness measurements could not be carried out in the cross-sectional plane, due to the very thin layer of the affected near-surface region). Fig. 15 also shows the very high standard deviations in the delamination phase as a result of valuable

heterogeneity within the wear track, expressed in terms of the topography and the corresponding phase fractions. Very high values of the hardness can be measured in the positions of the furrows (without surface delamination) compared to the much lower microhardness measured in the neighbouring delaminated regions.

3.4. Barkhausen noise measurements

The MBN detection device employed in this study could not detect the MBN signal from a matrix containing a martensite fraction of below 3% (based on previous experience with an applied Helmut Fischer Feritscope). Low-amplitude pulses originating from the surface may be detected, but it is not possible to distinguish these from the background
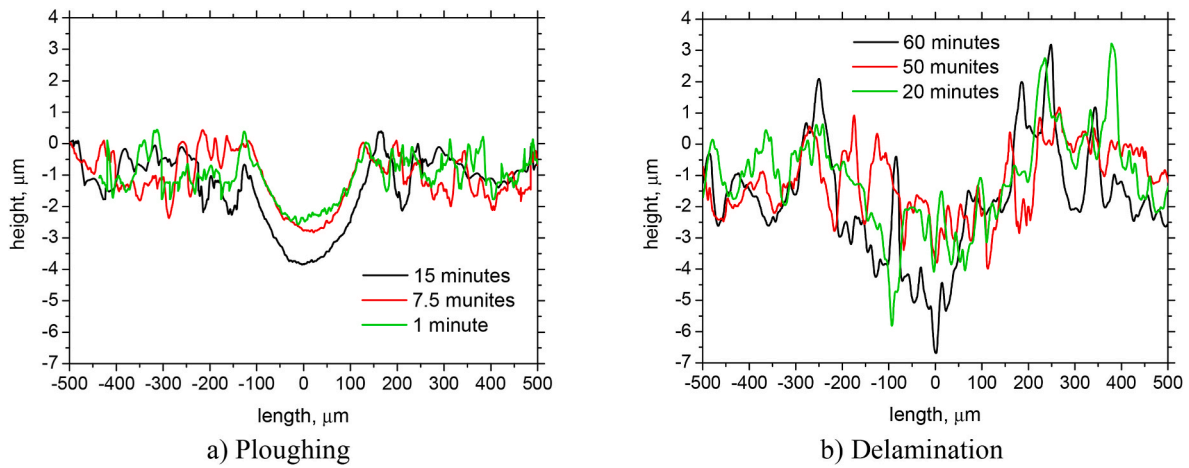
a) Ploughing

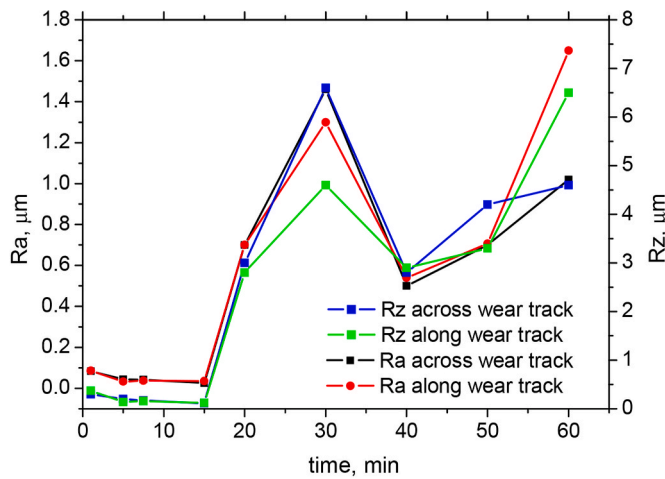b) Delamination

Fig. 9. Wear track profiles.

Fig. 10. Evolution of *Ra* and *Rz* across as well as along the wear track.

noise [13]. As soon as the austenite - martensite phase transformation becomes more developed and the martensite fraction exceeds a certain threshold, the distinct emission of MBN originating from the surface can be observed. Fig. 16 shows that the MBN increases with the martensite fraction, and its evolution is mainly driven by the increasing fraction of the ferromagnetic phase embedded in the paramagnetic austenite.

Again, a moderate increase in MBN in the ploughing phase is followed by abrupt growth at the ploughing - delamination transition. A progressive increase in MBN can be observed over the entire period of the experiment, unlike the evolution of the martensite fraction, especially in the final phases of the test (a decreasing martensite fraction is detected from the XRD patterns, see Fig. 12).

However, the evolution of the number of MBN pulses is slightly different. The number of pulses in the ploughing and delamination phase changes slowly, but an abrupt increase can be seen in the ploughing - delamination transition (see Fig. 16). The effective (rms) value of the MBN depends on the number of MBN pulses *n* and their magnitude X_i, as follows:

$$rms = \sqrt{\frac{1}{n} \sum_{i=1}^{n} X_i^2} \tag{5}$$

As there are almost constant numbers of the detected electromagnetic pulses in the ploughing and delamination phases but an increase in the detected MBN, it can be concluded that the increase in MBN in these phases is mainly due to the higher amplitudes of these pulses. It is also worth noting that the individual contribution of each DW in motion cannot be detected in this particular case (especially with respect to equation (5)) since DWs are clustered and occur in the form of avalanches [30]. Therefore, individually detected electromagnetic pulses can contain information from multiple DWs in motion. Moreover, due to the limited sampling frequency of the MBN signal (6.7 MHz), certain pulses may overlap in time.
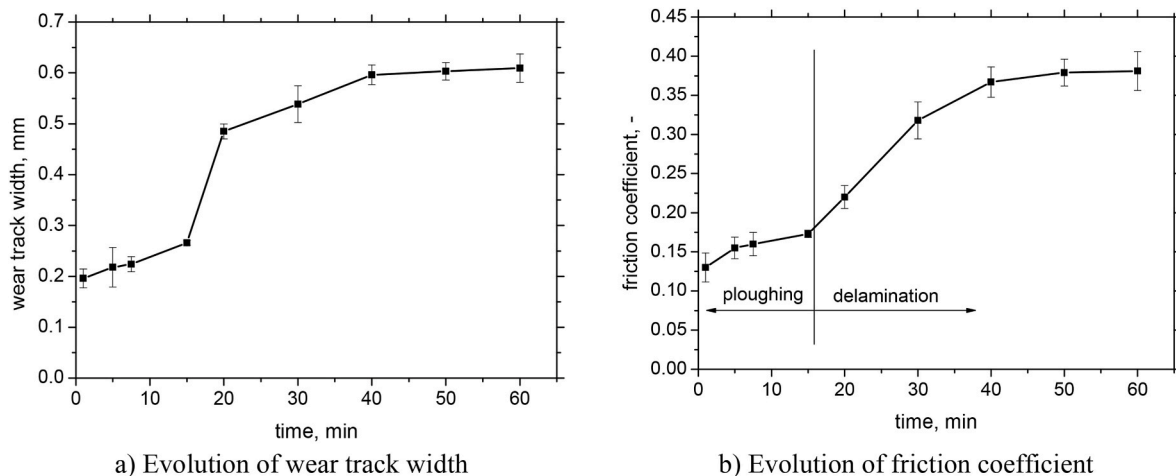

a) Evolution of wear track width

b) Evolution of friction coefficient

Fig. 11. Evolution of the wear track width and friction coefficient over the friction period.
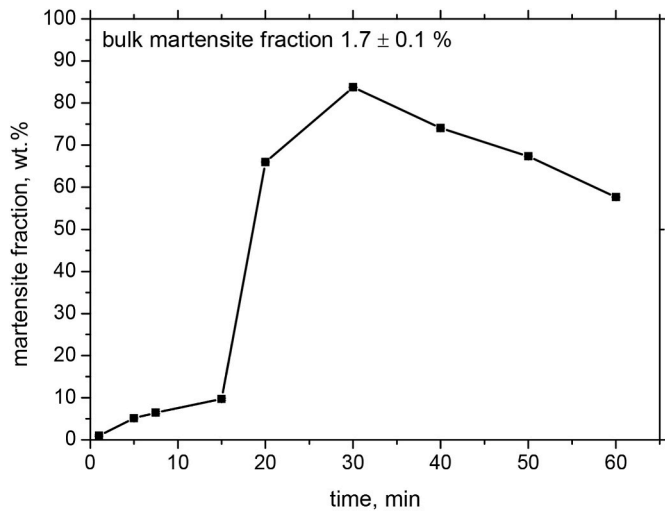
Fig. 12. Evolution of the martensite fraction over time under friction.

The evolution of the *PP* parameter is similar to that of the number of MBN pulses (see Fig. 17). *PP* changes at the ploughing - delamination transition, unlike *FWHM,* which exhibits a continuous decrease over the whole friction process. The MBN envelopes become narrower, and their height strongly correlates with the detected MBN. This narrowing of the MBN envelopes and the corresponding decrease in *FWHM* indicate that the conditions under which irreversible motion of the DWs is initiated, and the nature of their interactions with lattice imperfections, are becoming more similar.

It is known that an increase in the height of surface irregularities can contribute to a decrease in MBN [27]. The increasing wear track width and the corresponding depth make the transition of electromagnetic pulses from the investigated surface towards the sensing coil more difficult. However, this effect is minor since the detected MBN rises despite the increasing depth and width of the wear track.

Significant surface oxidation was also detected. Fe oxides are either paramagnetic or hard ferromagnetic phases [12], and their domain structure cannot be unpinned by the limited strength of the magnetic fields produced by the sensor. For these reasons, matrix oxidation usually attenuates MBN [31]. Again, this effect is only marginal since the detected MBN increased despite greater surface oxidation. It seems that the near-surface layer containing Fe oxides (as discussed in Section 3.1) is a relatively thin layer with respect to the MBN sensing depth, and the bulk of the martensite is unaffected by this phenomenon.

MBN is also a function of the stress state (in this case, macroscopic

residual stresses), as compressive stresses attenuate MBN [10–12,21]. Paramagnetic austenite is out of scope. A comparison of the evolution of the residual stresses in martensite (Fig. 13a) and the MBN (Fig. 16) clearly shows that the contribution of residual stresses to the MBN emission is small. The almost constant crystallite size in martensite (Fig. 13b) is another indicator that the magnetic pinning strength in this phase is not altered. Hence, the detected MBN is mostly dependent on the volume fraction of martensite.

Finally, the controversy between the increase in MBN and the decrease in martensite fraction observed from the XRD patterns in the final phases of the delamination phase needs to be explained. We assume that the decreasing martensite fraction is due to a combination of two effects. The first is a decreasing contact pressure (associated with the increasing width and depth of the wear track). The second is martensite tempering due to friction heating when the martensite layer in the wear track becomes stable enough and capable of withstanding the exerted load. The thermal softening effect can be proved by the decreasing dislocation density in austenite and the increasing crystallite size beyond 30 min, as well as the decreasing *HV0.2*, see also Figs. 13b, 14 and 15a. Moreover, it is considered that a certain fraction of martensite can be delaminated along with the increasing wear track size.

The area irradiated by XRD had a length in the range of 3–8 mm (according to the experimental geometry) and a constant width of 0.4 mm. Hence, the width of the irradiated area was higher than the width of the wear track in the ploughing phase (see Fig. 18), and the growth in the martensite fraction in this phase is due to the superimposed
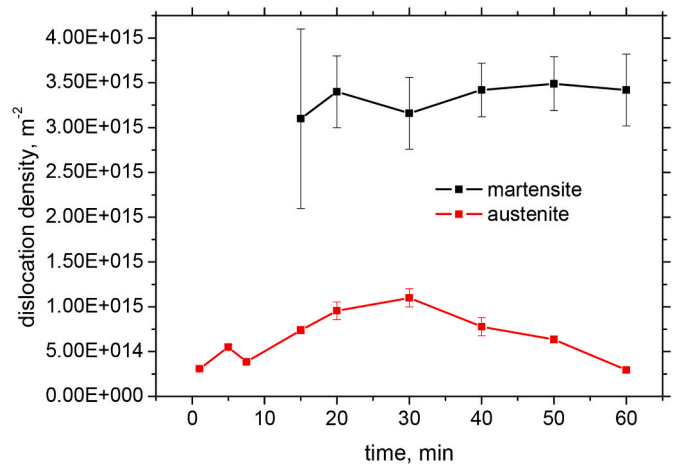

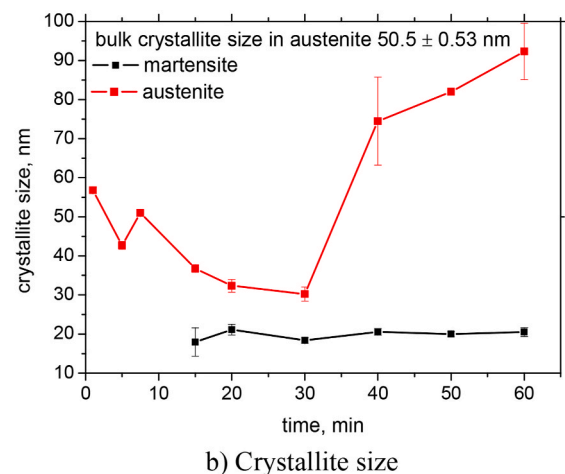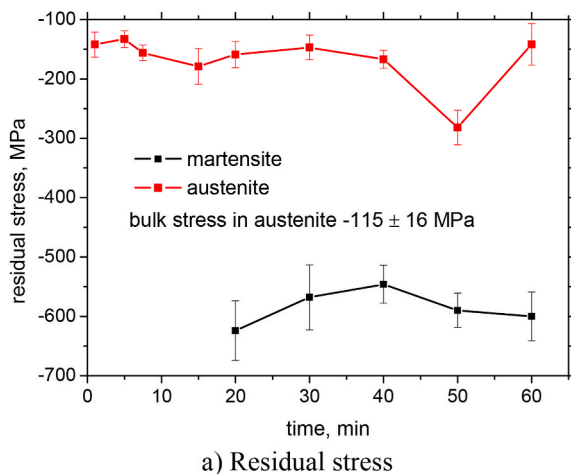**Fig. 14.** Evolution of dislocation density over time.

a) Residual stress

b) Crystallite size

Fig. 13. Evolution of residual stress and crystallite size over time.

a) Evolution of *HV0.2*
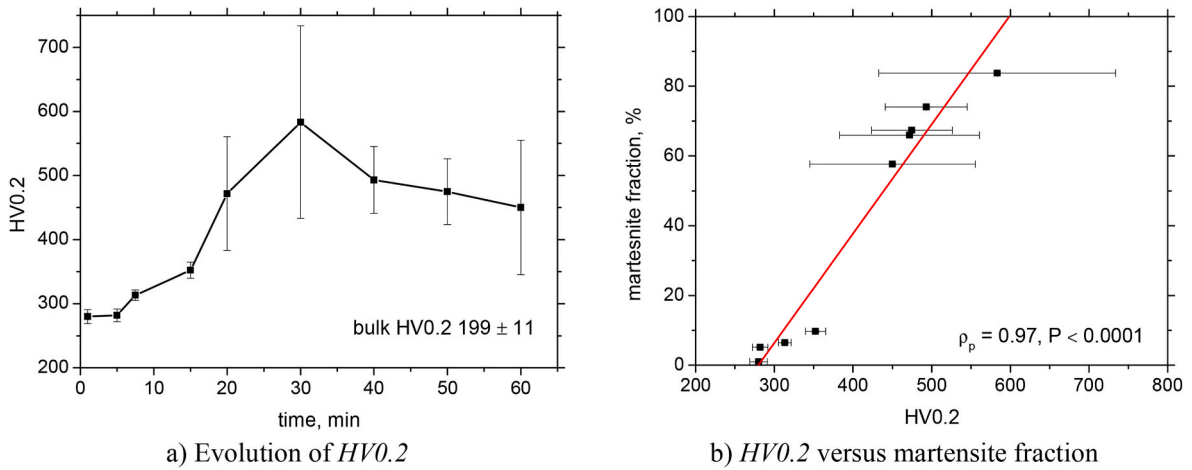
b) *HV0.2* versus martensite fraction

Fig. 15. Evolution of the *HV0.2* microhardness and its correlation with martensite fraction.
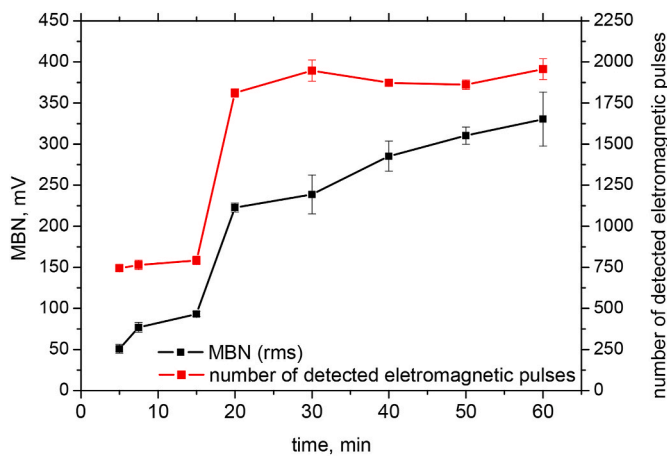

Fig. 16. MBN and number of detected electromagnetic pulses as a function of time under friction.

contribution of the increasing wear track width. The width of the irradiated area in the delamination phase is smaller than the width of the wear track (see Fig. 18) and hence does not play any role in this effect. The martensite fraction is driven by the degree of phase transformation and its depth. Moreover, the XRD sensing depth is below the thickness of the layer in which strain induced martensite can be found (see Fig. 6b).

The increase in MBN with the decreasing martensite fraction is therefore due to the much wider sensing area used by the MBN sensor (about 2×2 mm), see Fig. 19 (further details with respect of the sensor – dimensions as well as its shape can be found in Ref. [31]. Despite the decreasing martensite fraction detected by XRD, the MBN grows due to the increasing wear track width. In other words, the reduced martensite fraction is compensated by the increase in the affected area. Moreover, the MBN sensing depth is one order higher than the XRD technique [32, 33]. Therefore, the greater extent of strain-induced martensite to the depth (5–10 μm as aforementioned) contributes to the MBN signal strength as contrasted against the XRD technique.
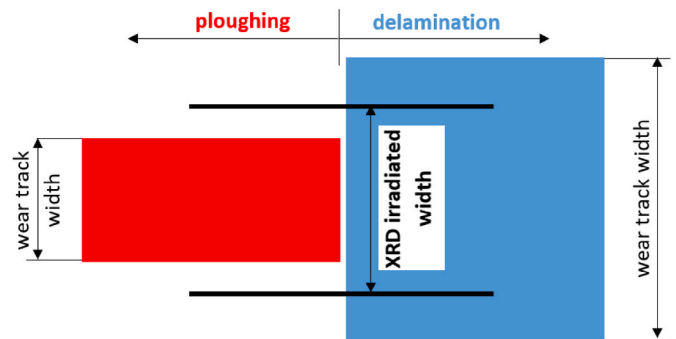

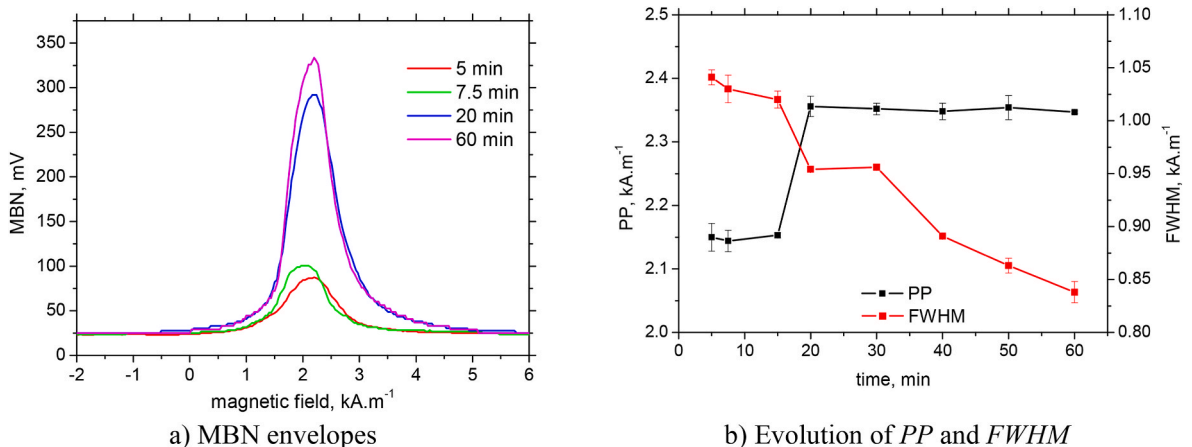**Fig. 18.** Wear track width versus XRD irradiated width – top view.

a) MBN envelopes

b) Evolution of *PP* and *FWHM*

Fig. 17. Changes in the MBN envelopes and evolution of *PP* and *FWHM* over time.
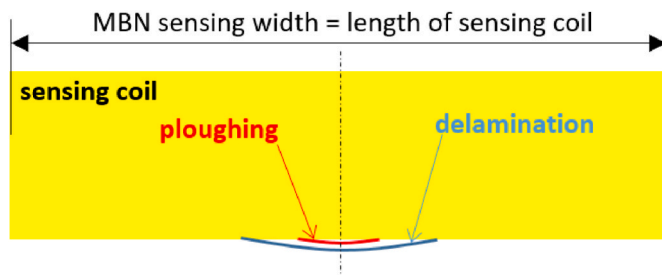
Fig. 19. Wear track width versus MBN sensing width – cross-sectional view.

A certain idea about stress distribution provides Fig. 8b or/and Fig. 9b, which indicate that the contact stress tends to grow from the edge of the wear track towards its centre. We expect that the martensite fraction and its depth will follow this distribution. However, this type of investigation is a challenging task since both XRD and the MBN detection technique provide average values, in which the contribution from martensite is integrated over the width of the wear track (or over the irradiated width if it is less than the wear track width).

4. Conclusions

The main findings of this study can be summarised as follows:

- Strain hardening of austenite is the predominant strengthening mechanism in the wear track in the ploughing phase;
- The ploughing - delamination transition significantly increases the size of the wear track, the fraction of martensite and the friction coefficient;
- The valuable martensite strengthening provides more stable opposition to friction load than that due to the strain hardening of austenite;
- MBN is sensitive to both the fraction and the quantity of martensite, particularly with respect to its effective value and *FWHM*.

The MBN technique, therefore, seems to be a suitable tool for monitoring the strain-induced martensite transformation that arises under friction and developed wear of austenite steels. The large sensing area and sensing depth of MBN mean that this technique is capable of detecting the austenite - martensite phase transformation, even at much higher loads and under a range of conditions that were not investigated in this study.

CRediT authorship contribution statement

M. Neslušan: Conceptualization, Data curation, Funding acquisition, Investigation, Methodology, Project administration, Supervision, Writing – original draft, Writing – review & editing. **J. Bronček:** Conceptualization, Formal analysis, Methodology, Project administration, Resources, Supervision. **P. Minárik:** Data curation, Investigation, Software, Visualization. **J. Čapek:** Data curation, Funding acquisition, Investigation, Software. **M. Vicen:** Data curation, Validation, Visualization. **M. Drbúl:** Investigation, Software, Validation.

Declaration of competing interest

The authors declare that they have no known competing financial interests or personal relationships that could have appeared to influence the work reported in this paper.

Data availability

Data will be made available on request.

References

[1] H. Berns, V. Gavriljuk, S. Riedner, High Interstitial Stainless Steels, first ed., Springer: Berlin/Heidlberg, Germany, 2012 https://doi.org/10.1007/978-3-642-33701-7_2.
[2] N. Fonstein, Advanced High Strength Sheet Steels, first ed., Springer International publishing, Switzerland, 2015 https://doi.org/10.1007/978-3-319-19165-2.
[3] R.E. Smallman, A.H.W. Ngan, Modern Physical Metalugry, eighth ed., Butterworth-Heinemann, Amsterdam, 2014.
[4] P. Haušild, K. Kolařík, M. Karlík, Characterisation of strain-induced martensitic transformation in A301 stainless steel by Barkhausen noise measurement, Mater. Des. 44 (2013) 548–554, https://doi.org/10.1016/j.jmatdes.2012.08.058.
[5] P. Haušild, V. Davydov, J. Drahokoupil, M. Landa, P. Pilvin, Characterisation of strain-induced martensitic transformation in a metastable stainless steel, Mater. Des. 31 (2010) 548–554, https://doi.org/10.1016/j.jmatdes.2009.11.008.
[6] P.L. Mangonon, G. Thomas, The martensite phases in 304 stainless steel, Metall. Trans. A 1 (1970) 1577–1578, https://doi.org/10.1007/BF02642003.
[7] S. Shukla, A.P. Patil, Effect of strain induced martensite reversal on the degree of sensitisation of metastable austenitic stainless steel, Procedia Struct. Integr. 14 (2019) 259–264, https://doi.org/10.1016/j.prostr.2019.05.033.
[8] X. Kleber, S.P. Barroso, Investigation of shot-peened austenitic stainless steel 304L by means of magnetic Barkhausen noise, Mater. Sci. Eng., A 527 (2010) 6046–6052, https://doi.org/10.1016/j.msea.2010.06.008, doi:.
[9] M.R.N. Astudilo, M.N. Nicolás, J. Ruzzante, M.P. Gómez, G.C. Ferrari, L. R. Padovese, M.I.L. Pumarega, Correlation between martensitic phase transformation and magnetic Barkhausen noise of AISI 304 steel, Proc. Mater. Sci. 9 (2015) 435–443, https://doi.org/10.1016/j.mspro.2015.05.014.
[10] S. Chikazumi, Physics of Ferromagnetism, second ed., Oxford University Press, Oxford, 2005.
[11] B.D. Cullity, C.D. Graham, Introduction to the Magnetic Materials, second ed., IEEE Press, New Jersey, 2009.
[12] D. Jiles, Introduction to Magnetism and Magnetic Materials, third ed., Taylor & Francis Group, New York, 2016.
[13] D. Blažek, M. Neslušan, M. Mičica, J. Pištora, Extraction of Barkhausen noise from the measured raw signal in high-frequency regimes, Measure 94 (2016) 456–463, https://doi.org/10.1016/j.measurement.2016.08.022.
[14] A. Beek, Advanced Engineering and Reliability, fisrt ed., TU Delft, The Netherlands, 2006.
[15] W. Hübner, A. Pyzalla, K. Assmus, E. Wild, T. Wroblewski, Phase stability of AISI 304 stainless steel during sliding wear at extremely low temperatures, Wear 255 (2003) 476–480, https://doi.org/10.1016/S0043-1648(03)00164-9.
[16] W. Hübner, Phase transformations in austenitic stainless steels during low temperature tribological stressing, Tribol. Int. 34 (2001) 231–236. S0301-679X (01)00006-8.
[17] K.L. Hsu, T.M. Ahn, D.A. Rigney, Friction, wear and microstructure of unlubricated austenitic stainless steel, Wear 60 (1980) 13–37, https://doi.org/10.1016/0043-1648(80)90247-1.
[18] Z.Y. Yang, M.G.S. Naylor, D.A. Rigney, Sliding wear of 304 and 310 stainless steel, Wear 105 (1985) 73–86, https://doi.org/10.1016/0043-1648(85)90007-9.
[19] M. Hua, X. Wei, J. Li, Friction and wear behavior of SUS 304 austenitic stainless steel against Al$_2$O$_3$ ceramic ball under relative high load, Wear 265 (2008) 799–810, https://doi.org/10.1016/j.wear.2008.01.017.
[20] X. Yan, J. Hu, H. Yu, Ch Wang, W. Xu, Unraveling the significant role of retained austenite on the dry sliding wear behavior of medium manganese steel, Wear 476 (2021), 203745, https://doi.org/10.1016/j.wear.2021.203745.
[21] X. Yan, J. Hu, L. Wang, Z. Chai, W. Sun, W. Xu, The coupled effect of thermal and mechanical stabilities of austenite on the wear resistance in a 0.2C–5Mn-1.6Si steel down to cryogenic temperatures, Wear (2021) 486–487, https://doi.org/10.1016/j.wear.2021.204116, 204116.
[22] J. Liu, G.Y. Tian, B. Gao, K. Zeng, Y. Zheng, J. Chen, Micro-macro characteristics between domain wall motion and magnetic Barkhausen noise under tensile stress, J. Magn. Magn Mater. 493 (2020) 165719, https://doi.org/10.1016/j.jmmm.2019.165719.
[23] A. Sorsa, S. Santa-aho, J. Wartiainen, L. Souminen, M. Vippola, K. Leviskä, Effect of shot peening parameters to residual stress profiles and Barkhausen noise, J. Nondestr. Eval. 37 (2018) 10, 1–11.
[24] M. Neslušan, P. Minárik, J. Grenčík, K. Trojan, K. Zgútová, Non-destructive evaluation of the railway wheel surface damage after long-term operation via

Barkhausen noise technique, Wear 420–421 (2019) 195–206, https://doi.org/10.1016/j.wear.2018.10.0146.

[25] M. Neslušan, J. Čížek, K. Zgútová, P. Kejzlar, J. Šrámek, J. Čapek, P. Hruška, O. Melikhova, Microstructural transformation of a rail surface induced by severe thermoplastic deformation and its non-destructive monitoring via Barkhausen noise, Wear 402–403 (2018) 38–48, https://doi.org/10.1016/j.wear.2018.01.014.

[26] L. Piotrowski, B. Augustyniak, M. Chmielewski, Z. Kowalevski, Multiparameter analysis of the Barkhausen noise signal and its application for the assessment of plastic deformation level in 13HMF grade steel, Meas. Sci. Technol. 21 (2010), 115702, https://doi.org/10.1088/0957233/21/11/115702.

[27] Y. Deng, Z. Li, J. Chen, X. Qi, The effect of the structure characteristics on Magnetic Barkhausen noise in commercial steels, J. Magn. Magn Mater. 451 (2018) 276–282, https://doi.org/10.1016/j.jmmm.2017.11.041.

[28] G.K. Williamson, R.E. Smallman, Dislocation densities in some annealed and cold-worked metals from measurements on the X-ray debye-scherrer spectrum, Philos. Mag. A 1 (1955) 34–46, https://doi.org/10.1080/14786435608238074.

[29] K.L. Johnson, Contact Mechanics, ninth ed., Cambridge University press, Cambridge, 2003.

[30] G. Bertotti, Spacetime correlation properties of the magnetisation process and eddy current losses: applications. I. Fine wall spacing, J. Appl. Phys. 55 (1984) 4339, https://doi.org/10.1063/1.333001.

[31] M. Neslušan, F. Bahleda, P. Minárik, K. Zgútová, M. Jambor, Non-destructive monitoring of corrosion extent in steel rope wires via Barkhausen noise emission, J. Magn. Magn Mater. 484 (2019) 179–187, https://doi.org/10.1016/j.jmmm.2019.04.017.

[32] A. Stupakov, A. Perevertov, M. Neslušan, Reading depth of the magnetic Barkhausen noise. I. One phase semi-hard ribbons, J. Magn. Magn Mater. 513 (2020), 167086, https://doi.org/10.1016/j.jmmm.2020.167086.

[33] A. Stupakov, A. Perevertov, M. Neslušan, Reading depth of the magnetic Barkhausen noise. II. Two-phase surface-treated steels, J. Magn. Magn Mater. 513 (2020), 167239, https://doi.org/10.1016/j.jmmm.2020.167239.